

This manuscript is the originally submitted version of an article that has finally been published as:

Nicolas J. Peter, Christiane Gerlitzky, Abdulrahman Altin, Simon Wohletz, Waldemar Krieger, The Hai Tran, Christian H. Liebscher, Christina Scheu, Gerhard Dehm, Peter Groche, Andreas Erbe: Atomic level bonding mechanism in steel/aluminum joints produced by cold pressure welding. *Materialia*, 7, 100396 (2019). DOI: 10.1016/j.mtla.2019.100396

Final published version of the manuscript is available from:

<https://doi.org/10.1016/j.mtla.2019.100396>

Atomic level bonding mechanism in steel/aluminum joints produced by cold pressure welding

Nicolas J. Peter¹, Christiane Gerlitzky², Abdulrahman Altin¹, Simon Wohletz²,
Waldemar Krieger¹, The Hai Tran¹, Christian H. Liebscher¹, Christina Scheu¹, Gerhard
Dehm¹, Peter Groche² & Andreas Erbe^{1,3,§}

¹Max-Planck-Institut für Eisenforschung GmbH, 40237 Düsseldorf, Germany

²Technische Universität Darmstadt, Institute for Production Engineering and Forming Machines, 64287
Darmstadt, Germany

³NTNU, Norwegian University of Science and Technology, Department of Materials Science and
Engineering, 7491 Trondheim, Norway

[§] Corresponding author

Keywords: Cold welding; scanning transmission electron microscopy; electron energy
loss spectroscopy; aluminum steel joints; interfacial bonding;

Abstract

Cold pressure welding of aluminum alloys and steels offers an attractive opportunity of cost-effective joining of components made of two important structural materials classes. This work shows results of an investigation of joints between an aluminum alloy (EN AW6082) and a carbon steel (C15) produced by cold extrusion welding. Mechanical testing under tensile loads revealed site specific interface strength to be between 30 to 60 % of the constituent materials' strengths. However, investigation of the fracture surfaces indicates that interface strengths can exceed the aluminum alloy's strength in areas where the bonding process substantially enlarged the Fe-Al interface region, due to the welding geometry. Near atomic scale resolution investigations of the interface using

aberration-corrected scanning transmission electron microscopy combined with electron energy loss spectroscopy disclose two different regions along the cold pressure welded interface. The majority of the interfacial area is oxygen free with Fe-based and Al-based crystals joining at the interface. No intermetallic phase was identified. However, results show Fe-Al interface bonding with a covalent bond characteristic in the Al-L_{2,3} edge, to which interface adhesion is attributed. In addition, a small fraction of the steel/aluminum interface was covered with oxidic regions of about 10 nm thickness in electron microscopy samples. This oxide is predominantly an amorphous aluminum oxide, with only few Fe-O bonds. Based on the findings of the present paper, an extended Bay model of metallurgical bond formation at near atomic level is presented in which the interfacial bonding characteristics of the applied cold pressure welding process is accounted for.

Introduction

Multi-material design allows locally adapted physical properties of metals, such as conductivity [1] and targeted weight reduction of construction materials at the same time [2]. Combining aluminum and steel, the most commonly used construction materials in mechanical engineering, could be used to improve component strength, while at the same time reducing component weight [3], or improving corrosion resistance [4]. However, classical heat induced welding processes of this material combination typically result in the formation of one of the Fe-Al intermetallic phases as interfacial

connection [5,6]. These intermetallics are usually strong but brittle solids at low temperatures and under ambient conditions [7] and consequently promote failure of the joint materials along that interface at low strains. This weakening influence was found to be governed by the base constituents and reported to occur above critical interface thicknesses between 1.5 μm (Al with 5 wt. % Si alloy) and 7 μm (for 99.5 wt. % pure Al) [5]. Consequently, significant efforts are being made on the development of joining technologies by plastic deformation without heat induction to avoid intermetallic phase formation [8].

A widely spread solid joining technology is accumulative roll bonding. The bonding mechanism involved in that process was theoretically described on a macroscopic level in the late 1970s by Bay [9]. According to Bay's model, bonding occurs under ambient conditions by a sequence of events. First, thinning and breaking of brittle cover layers, as for example work hardened or metal oxide layers, occurs along with the material's surface expansion. Second, after exceeding a critical threshold of surface expansion, uncoated and reactive juvenile metal extrudes between these cracks and finally results in bond formation with the normal pressure of the interface being the second crucial parameter of the welding process. The surface expansion threshold depends on the metal combination and chosen surface preparation [10,11] and therefore influences the bond strength significantly. The model was modified by Cooper and Allwood by stating that in addition to the natural oxide layer, entrapped air between the joining surfaces contributes to the macroscopic properties of the joint [12]. This air has been described to oxidize exposed pure metal surfaces after exceeding Bay's critical surface expansion.

Thereby, it is claimed to lead to an increased threshold before a bi-material bond can be established. The authors refer to a study of Barlow et al. [13], visualizing the dispersion of plate-like native oxide fragments along the interfaces of cold roll bonded aluminum alloy sheets (AA8011) by transmission electron microscopy (TEM), to support their extended theory. In contrast, for friction stir welded multi material joints out of copper (CW008A) and aluminum (AA1050), Marstatt et al. show a discontinuous intermetallic phase extending about 50 nm from the interface after processing at a rotation speed of 800 min^{-1} [14]. Under these conditions, maximum temperatures during the process are $\sim 280 \text{ }^\circ\text{C}$ in the two constituent sheets. No residual oxides were detected with energy dispersive X-ray spectrometry (EDS) after welding. Tensile tests of the welds, however, revealed minimal interface strengths. Only with increasing rotational speed, consequently applying higher temperature, a continuous, intermetallic and semicoherent film was established leading to the conclusion that for the Al-Cu system, bonding occurs mainly through the intermetallic interface layer [14]. A different picture is drawn for the much more challenging Fe-Al system studied recently by Wang et al. [15]. The interface of aluminum and steel cold roll bonded samples displays an amorphous interface region of 2 nm thickness. It was assumed that this interface is due to Fe diffusion into Al but frozen due to only a low temperature increase in fractions of a second of exposure during the process. However, diffusion profiles show no hint of intermetallic compounds being formed and the origin of the beneficial contribution towards increased bond strength is not discussed in detail.

Cold forging by cold extrusion of aluminum (EN AW6082 – 3.2315) and steel (C15 – 1.0401), yielded a continuous 2-3 nm thick interfacial reaction layer for Altin et al. [16]. However, the presented chemical composition across the interface lacks resolution and is not unambiguously related to an intermetallic phase. In addition, reduced intensity in high angle annular dark field (HAADF) scanning transmission electron microscopy (STEM) images of features at the interface is not uniquely related to an intermetallic phase as claimed to be present, but could be due to an inclined interface, which would correlate with the given EDS composition profiles. These samples revealed a good maximum tensile strength of ~200 MPa. The good efficiency of this cold extrusion process is also reflected in a recent study by Wohletz and Groche, who observed best tensile strengths of that system for room temperature bonding and similar strengths when joining the specimens at elevated temperatures reaching up to 600 °C [17]. Wohletz showed further that for different surface preparations the bond strengths can exceed the strength of the weaker aluminum alloy. An especially beneficial surface preparation consists of brushing or etching [18].

In summary, joining by cold forging [19] offers highly attractive opportunities for strong bonds of components consisting of different metals. Crucial technological conditions, especially sufficient surface expansion, level of normal stresses acting on the interface and adequate surface preparations have to be respected. So far, design criteria for cold pressure welding processes have been gained empirically. Further improvements towards higher reliability of the process require deeper investigations of the bonding mechanism.

In particular, the role of oxides seems to be an important aspect of the chemical

analysis. So far, EDS and standard high-resolution techniques were mainly applied. Advanced analytical and structural tools have not been used to their full potential, yet. Therefore, in the present work, the bonding situation of cold forged joints between aluminum and steel is investigated for a Fe-Al system [16] by means of aberration-corrected scanning TEM (STEM). The cold pressure welding mechanism differs drastically from phenomena occurring during mechanical and force-closed joining by plastic deformation [20]. In the following the chemical nature of the formed bonds at the interface is examined in further detail by making use of electron energy loss spectroscopy (EELS), and correlations with the interface strength evaluated by mechanical testing of the samples.

Experimental

The process chain from the semi-finished metal blanks to the completely welded product is shown in Figure 1. Cylindrical aluminum (EN AW6082 – 3.2315) and steel (C15 – 1.0401) blanks are machined to a diameter of 41.5 mm and a height of 15 mm. Their flow stresses are then adjusted by a primary heat treatment to be as equal as possible (Figure 1a). Heat treatment has proven to be a crucial step in welding by cold forging of aluminum and steel in our previous work [21]. After heat treatment, aluminum is in an artificially aged T6 state, while the steel is spheroidized.

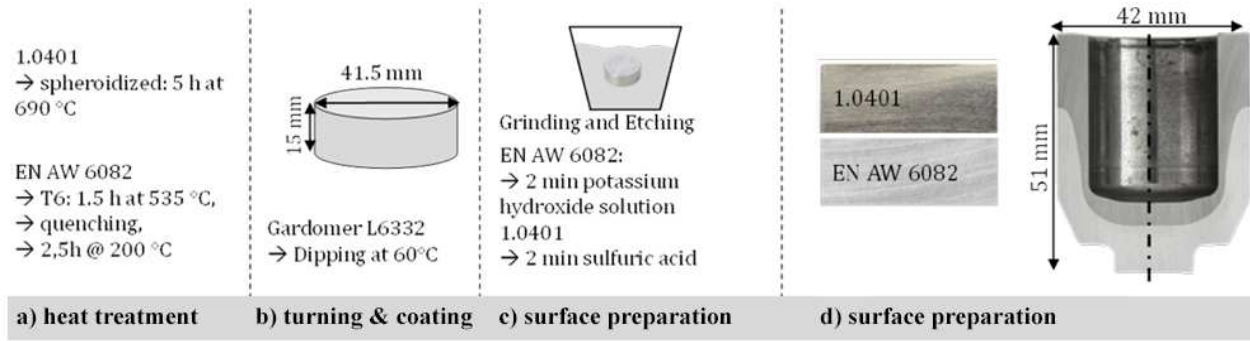


Figure 1: Process chain for the employed cold pressure welding by an extrusion welding process.

a), heat treatment, b) turning and coating, c) chemical surface preparation, d) joining process

Joining the metal blanks is performed as described in detail in [21], starting with a targeted surface preparation sequence. First, the blanks are mechanically ground, which resulted in a final root mean square surface roughness of 0.08 μm and 0.17 μm for steel and aluminum, respectively. Secondly, the blanks are coated entirely, except at the surfaces to be joined, with a solid polymer lubricant, Gardomer® L 6332, Chemetall (Figure 1b). Directly before the joining process, all non-coated surfaces are chemically and electrochemically treated (Figure 1c). The aluminum surface is degreased in a 10 % aqueous potassium hydroxide solution for 2 min, followed by a water rinsing step. A subsequent pickling step was performed by dipping the billet in an aqueous 10 % nitric acid for another 2 min. The steel surface, on the other hand, is electrochemically treated for 2 min in a 10 % sulfuric acid applying a current of -4.5 A to ensure a maximum possible reduction of oxides. Afterwards, the exposed aluminum and steel surfaces were washed with distilled water, cleaned with technical grade ethanol and dried. Finally, the steel and aluminum cylinders are stacked on top of each other (Fe on the top, Al at the bottom) and joined through a cold extrusion process, as shown in Figure 1d.

After joining, the resulting bi-material samples were mechanically and microstructurally investigated. The mechanical testing geometries are sketched in Figure 2. From a joined sample (Figure 2a) two 2 mm thick cross-sections were extracted for macroscopic testing (Figure 2b). These tests are combined with scanning electron microscopy (SEM) investigations of the remaining fracture surfaces at five distinct locations indicated by arrows in Figure 2b). The interface close to local micro tensile testing sites (locations 1 and 2 in Figure 2c) is further investigated using STEM and related methods at chosen locations of best performance (location 3 in Figure 2c). For macro tensile tests the cross-section is pulled apart parallel to the extrusion direction leading to a complex loading condition of the joint area (mixed normal stress and shear stress for different parts). Afterwards the steel side of the parted sample is observed in a JEOL JSM6610LV SEM (backscatter micrographs) in order to quantitatively determine the amount of Al alloy remnants. Thereby the location of best interfacial bonding is identified by the amount of Al remnants, which originate from Al bulk failure instead of interface failure. Micro tensile tests were performed at two distinct positions at the bottom of the joined sample highlighted in Figure 2c along with the testing geometry. For these tests a more defined loading condition is achieved with the interface being orientated perpendicular to the loading direction and thus mainly normal stress acting on the interface and the ultimate tensile strength (UTS) determined. The testing samples were prepared with a wire eroding machine. The locations with high surface expansion and high amounts of Al remnants on the fracture surface were analyzed. However, the area of highest surface

expansion with almost full coverage of Al remnants was not accessible for micro tensile testing due to the limited amount of material given by the extrusion geometry.

From the area of highest surface expansion STEM samples were prepared to investigate the microstructure and bonding (location 3 in Figure 2 c). Cross-sectional lamellae were extracted via a Thermo Fischer Scientific Helios 600i focused ion beam machine. The final thinning step to achieve electron transparency was performed with an acceleration voltage of 5 kV to limit beam damage.

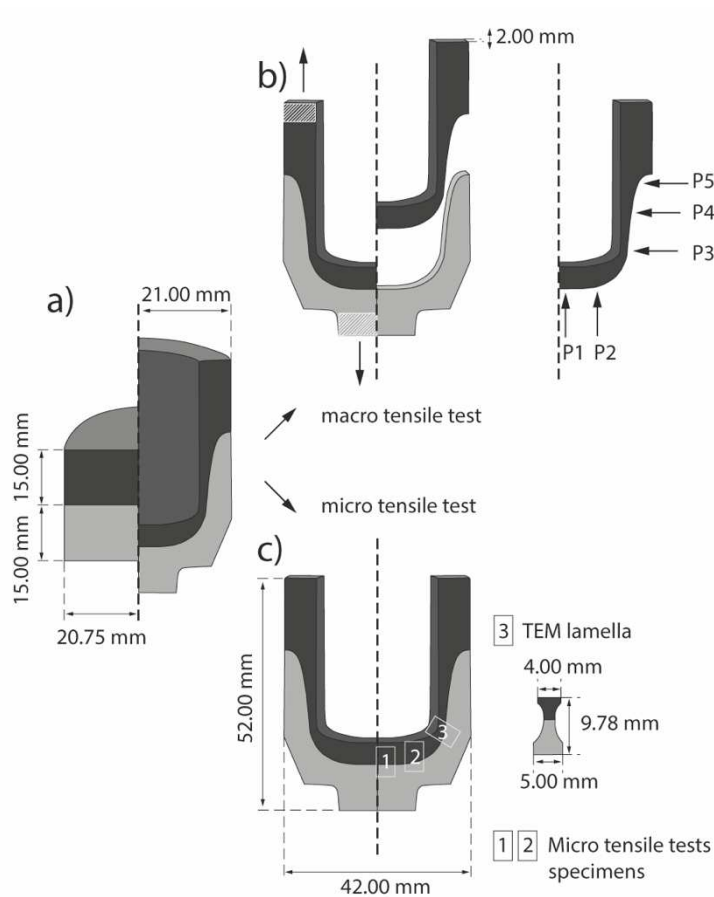


Figure 2: Characterization flow chart starting with a) samples before and after joining and followed by b) macro tensile extraction of samples and highlighted SEM analysis positions as

well as c) micro tensile testing at locations 1 and 2 as well as TEM analysis at highlighted location 3.

The prepared cross-sectional STEM lamella was studied in a probe-corrected Thermo Fischer Scientific Titan Themis 60-300 STEM at an acceleration voltage of 300 kV equipped with a high-brightness field emission gun (X-FEG). HAADF micrographs were acquired at a semi-convergence angle of 23.8 mrad and a semi-collection angle of 73-200 mrad with a beam current of about 80 pA. Analytical STEM methods included electron energy loss spectroscopy (EELS) and energy dispersive X-ray spectroscopy (EDS), which make use of the equipped Gatan GIF Quantum ERS energy filter at an energy resolution of ~ 1.1 eV (measured at the half width of the zero loss peak) and the ChemiSTEM Super-X detector system, respectively. EELS and EDS maps were recorded at two different positions along the cold welded bi-material interface with a drift correction running during acquisition. One site containing oxygen (interfacial oxide inclusion) and one oxygen-free location. While EDS maps of different elements were acquired at the same time, EELS maps were acquired in three consecutive steps at the exact same position for the respective elemental edges of interest, i.e. the Al-L_{2,3} edge (70 eV), Fe-L_{2,3} edge (705 eV) as well as the O-K edge (530 eV).

EELS spectral images were acquired with a pixel size of about 5 Å (oxygen-free location) and 12 Å (oxygen-containing location). The lamella's relative thickness t/λ , with λ as the material-dependent mean free path for inelastic scattering, was determined from the

acquired low loss signal, thanks to a Dual EELS measurement mode, and found to be thinner on the Al side but on both sides below 1. Therefore, no deconvolution method was applied to the recorded spectra. From the acquired spectral images, integrated signal maps were extracted to highlight areas of different elemental composition. The dispersion for the oxygen-lean EELS maps was chosen to 0.1 eV/channel, while the maps containing oxygen-rich interfaces were acquired at 0.25 eV/channel. The pre-edge background was subtracted using a power law fit before signal integration and energy-loss near-edge structure (ELNES) analysis. The latter procedure was used to get insights into the bonding state of the respective constituents at the bi-material interface in a spatial difference kind of manner. To that end, an area consisting of two pixel rows of the acquired maps was chosen to increase the spectrum intensity and thus signal-to-noise ratio in the steel, the Al-alloy and especially at the interface. The applied spatial difference technique makes use of the ELNES signal at the interface being a linear superposition of the weighted signals originating from atoms around and right at the interface [22]. Therefore, the method is capable of revealing interfacial ELNES structures associated to only few atoms at the very interface with coordination or oxidation state different from the bulk. Choosing areas of the same size at the same collection parameters allows for subtraction of the bulk contributions (I_a & I_b) from the interface signal (I_{int}) resulting in a so-called difference spectrum (I_{diff}) that can be described according to

$$I_{diff} = I \int e^{-\alpha I_a - \beta I_b} \quad (1)$$

with α and β being scaling factors to account for the relative amount of the respective bulk portion contributing to the interface spectrum. Details of this method are provided in [22].

EDS maps were acquired and analyzed by separating areas of distinct composition through a principal component analysis [23]. The individual elemental maps were combined to obtain comprehensive elemental information at the interface.

Results

Table 1 presents the results of the conducted micro tensile tests. For comparison, monolithic reference samples of the constituent alloys were tested additionally in micro tensile sample geometry along with specimens eroded out of the joint material (Figure 2c).

Table 1: Ultimate tensile strengths of the Al/Fe joints and the base materials including standard deviation

	Treated Steel	Treated Aluminum	Bi-material joint Position 1	Bi-material joint Position 2
Micro tensile strength (MPa)	484.9 ± 13.4	443.7 ± 4.6	145.2 ± 60.0	295.4 ± 35.6

The results reveal a higher variation for the bi-material samples compared to the monolithic references along with a reduced (interface) strength. However, the bi-material UTS rises from position 1 to position 2 and the standard deviation drops significantly. The bi-material joints were found to increase from 30 % to 60 % of the strength of the constituent materials from position 1 to position 2. The strongest sample exhibited a strength in position 2 of 345.4 MPa indicating a high relative strength of 78 % of the maximum reachable strength, i.e. the strength of the T6 aluminum.

Local SEM analysis of the fracture surface is performed to further understand the differences in the resulting interfacial bonding. Therefore, in order to establish a sound structure-property relationship, a first step was to analyze the fracture surface of macroscopically parted bi-material joints at five distinct locations along the interface (Figure 2b). SEM backscatter micrographs are presented in Figure 3 along with the respective area exposure of the investigated steel part (bright). Dark contrast represents Al-alloy remnants on the steel part. The micrographs are provided along with the locations highlighted on a bi-material joint's cross-section. In addition, the amount of exposed steel is plotted over all five observation locations in combination with the

correlated locally measured relative tensile strength to indirectly visualize the local interfacial integrity. Mechanical data is normalized to the micro tensile strength of the monolithic reference (compare Table2). The shaded region in the plot is where micro tensile test sample were extracted. The micrographs and quantitative coverage information reveal location three (P3) being covered almost entirely with Al-alloy remnants, while approaching the outer or inner part of the joint (P5, P1) the Al-alloy coverage is reduced significantly.

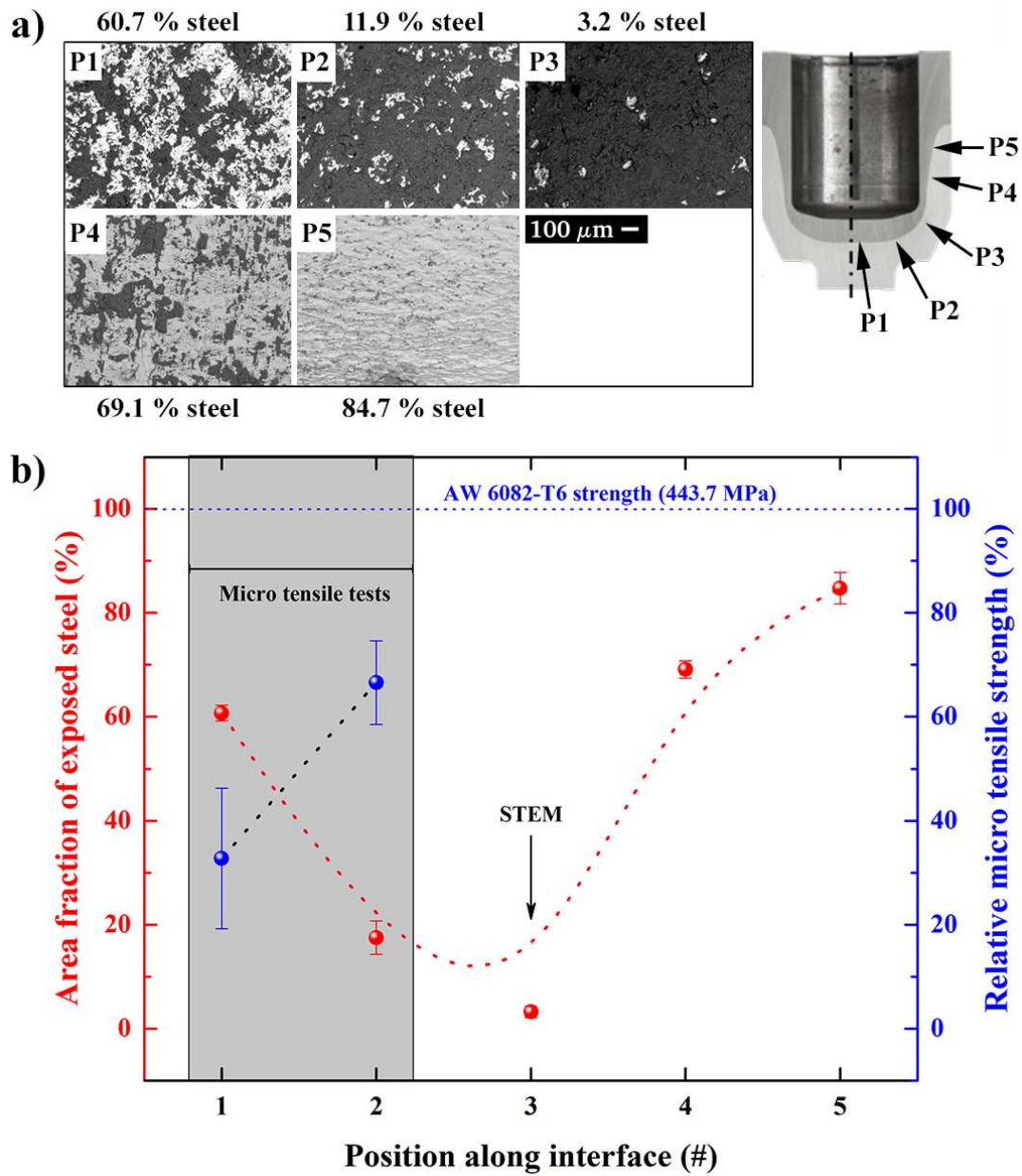


Figure 3: (a) SEM backscatter micrographs of fracture surface from macroscopically tensile tested joints. Top-down views onto the steel part of the fractured bi-material joint (dark: Al-alloy remnants, bright: steel remnants). (b) The exposed steel fraction of the micrographs is additionally plotted with a line approximation to guide the eye. In addition, the measured relative micro tensile strength of joints is plotted for the accessible locations to demonstrate the

trend of interface strength and thus the correlation between both. Mechanical data is normalized to the treated Al alloy's UTS given in Table 2 (443.7 MPa).

An overview STEM micrograph of an extracted lamella from location P3 (compare Figure 2b) is presented in Figure 4. HAADF Z-contrast imaging conditions were used (Figure 4b), separating the lamella into a dark and a bright region that can be related to the Al- and the Fe-based materials, respectively. Two distinct locations were identified close to the top of the lamella and in the middle of the lamella. The upper part appeared as a relatively flat interface at low magnification. At higher magnification and in zone axis orientation in the Fe part, linearly decreasing lattice plane intensities are observed over a region of 2 nm indicating that the interface is not oriented edge-on (Figure 4a). In addition, as there is no apparent low-index orientation relationship, no atomic columns are resolved on the aluminum side; it just appears dark. In contrast to the smooth upper and lower interface part, the central interface region appeared rough and wavy (Figure 4b). In close proximity to the interface at this position, features of intermediate image intensity are visible with a width on the order of about 20 nm (Figure 4c). Acquired EDS maps in these regions indicate the upper straight part of the interface being oxygen free down to lattice plane resolution (Figure 4a), while in the central, rougher part oxygen was detected at the interface (Figure 4c).

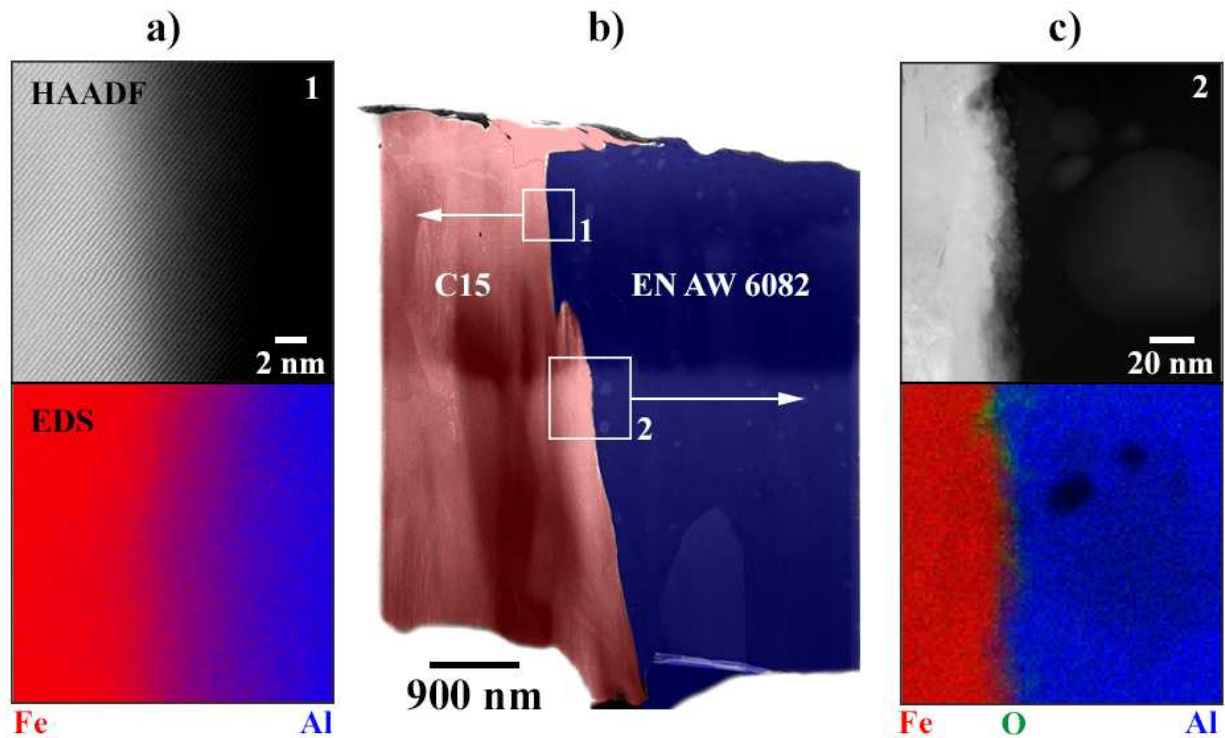


Figure 4: TEM lamella containing the bi-material interface. (a) Oxygen-free area with atomically resolved interface termination of the sample's steel part (HAADF STEM) along with the corresponding EDS map of that region. (b) Overview of the TEM lamella (HAADF STEM) with the Fe and Al part being highlighted in red and blue, respectively. Two distinct areas, 1 and 2, for closer investigation in (a) and (c) are highlighted. (c) Oxygen-containing medium contrast region (HAADF STEM) along with the corresponding EDS map of that region.

Additional analytical inspection of the two distinct boundaries is achieved by EELS measurements across the oxygen-free and -containing interface portions. At the supposedly oxygen-free interface segment, EELS mapping revealed little amounts of oxygen speckled randomly over the acquired map and a sharp interface (Figure 5a). In

contrast, confined oxygen containing features were identified by EELS mapping in agreement to the findings obtained by EDS mapping (Figure 5b). Fe and Al were additionally investigated by EELS and are visualized along with oxygen in RGB composite images.

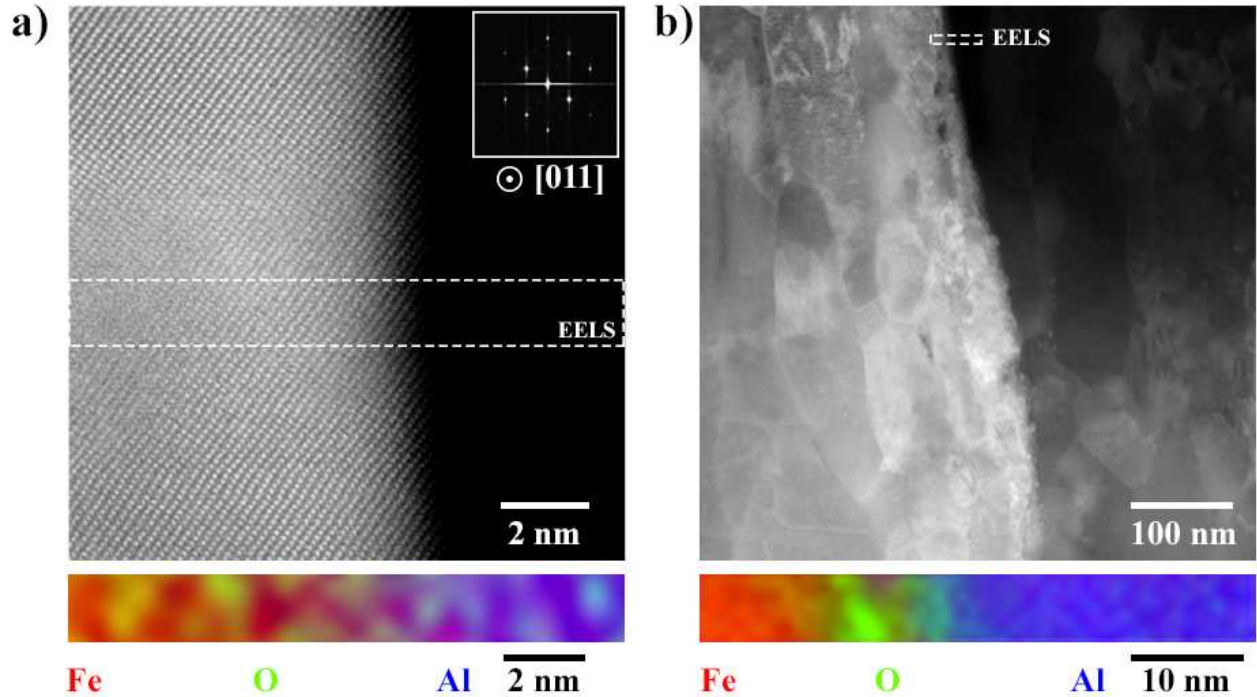


Figure 5: HAADF STEM images of the interface of the sharp oxygen-free interface (a) and the oxygen containing region (b) with their corresponding EELS maps (Fe in red, O in green, Al in blue).

To investigate the bonding states at the interface, EELS spectra were acquired, analyzed at the oxygen-free and oxygen-containing areas across the interface and compared against reference spectra acquired without monochromator at comparable energy resolution (~ 1 eV). Considering the Fe-L_{2,3} edge, the spectra collected on the Fe side of the lamella are presented in Figures 6 (a) for both distinct areas. Additionally, reference

19

Fe-L_{2,3} edges of pure Fe [24], hematite (Fe₂O₃) [24] and FeAl [25] are included, respectively. Clearly, the Fe edges of samples from the present study are almost identical for both distinct interface areas, match the reference spectra of pure Fe, and are distinctly different from the other reference spectra. The latter contain additional minor peaks compared to the edge of pure iron, which are not observed experimentally for the present system.

The O-K edge was recorded across the oxygen-containing interface region and is shown in Figure 6b) along with reference a spectrum of Fe₂O₃ [23] and references for the amorphous α -Al₂O₃ [27], γ -Al₂O₃ [27] as well as α -Al₂O₃ (measured in house [26]) polymorphs. All three reference spectra of the O-K edge were measured under similar conditions as in the present study in terms of energy resolution and dispersion. Comparison of the spectra indicates a strong resemblance of our measured spectrum with γ -Al₂O₃, not at all with α -Fe₂O₃. In addition, the oxygen bound at the interface appears more amorphous / γ -Al₂O₃ like compared to the α -Al₂O₃ spectrum, as the anisotropy of the first peak is not seen and the second peak appears to be a single maximum compared to the multiple peaks measured for the crystalline alumina reference [26].

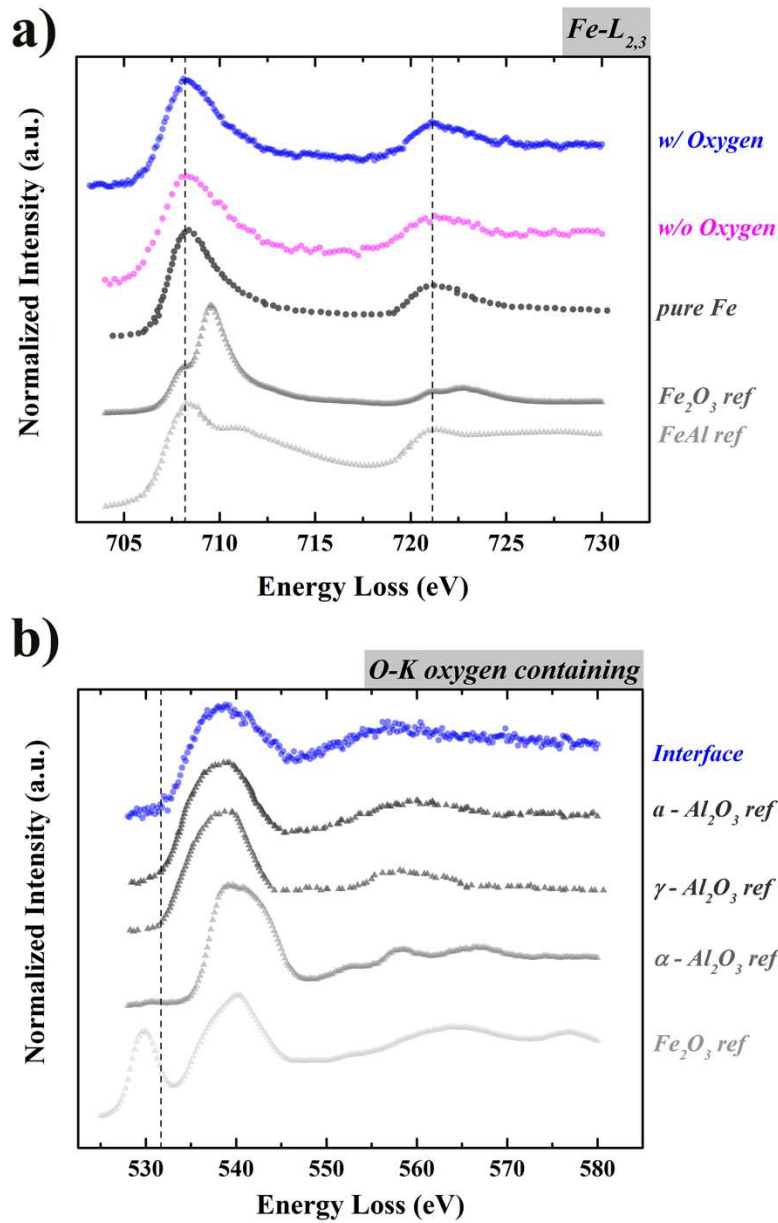


Figure 6: (a) Fe-L_{2,3} edge of the sample's Fe part in the oxygen present region and the oxygen free area as well as for a pure Fe reference [24], a Fe₂O₃ reference [24] and a FeAl reference [25]. (b) O-K edge recorded at the oxygen containing interfacial region along with a Fe₂O₃ reference (measured in house [23]), and references for α-Al₂O₃ [27], γ-Al₂O₃ [27] as well as α-Al₂O₃ (measured in house [26]).

The Al-L_{2,3} edge at the oxygen-rich interface is presented in Figure 7a) for the Al bulk, recorded across the interface, and along with the corresponding spatial difference spectrum at the interface. The difference spectrum at the interface has a distinctly different appearance compared to the pure Al edge in the bulk, indicating a bond formation to other atoms than Al at the interface. However, comparing it to the presented α -Al₂O₃ oxide reference edge, a close spectral course resemblance is observed. Especially the shoulder at edge onset around 76 eV indicated by arrows in Figure 7a) has to be noted, which only appears in the amorphous reference spectrum as well. All Al₂O₃ references were measured in-house [26].

Finally, the Al-L_{2,3} edges were also recorded at the oxygen free interface region (Figure 7b), in the bulk as internal reference and across the interface. The corresponding difference spectrum obtained at that location was distinctly different to the bulk edge but resembled more the FeAl reference state [28], rather than the Fe₃Al state [28]. Especially the initial slight intensity increase over the plateau region has to be noted for the difference spectrum (indicated by arrows). However, effects from sample thickness, like plasmon excitation, cannot be excluded entirely as cause for such features.

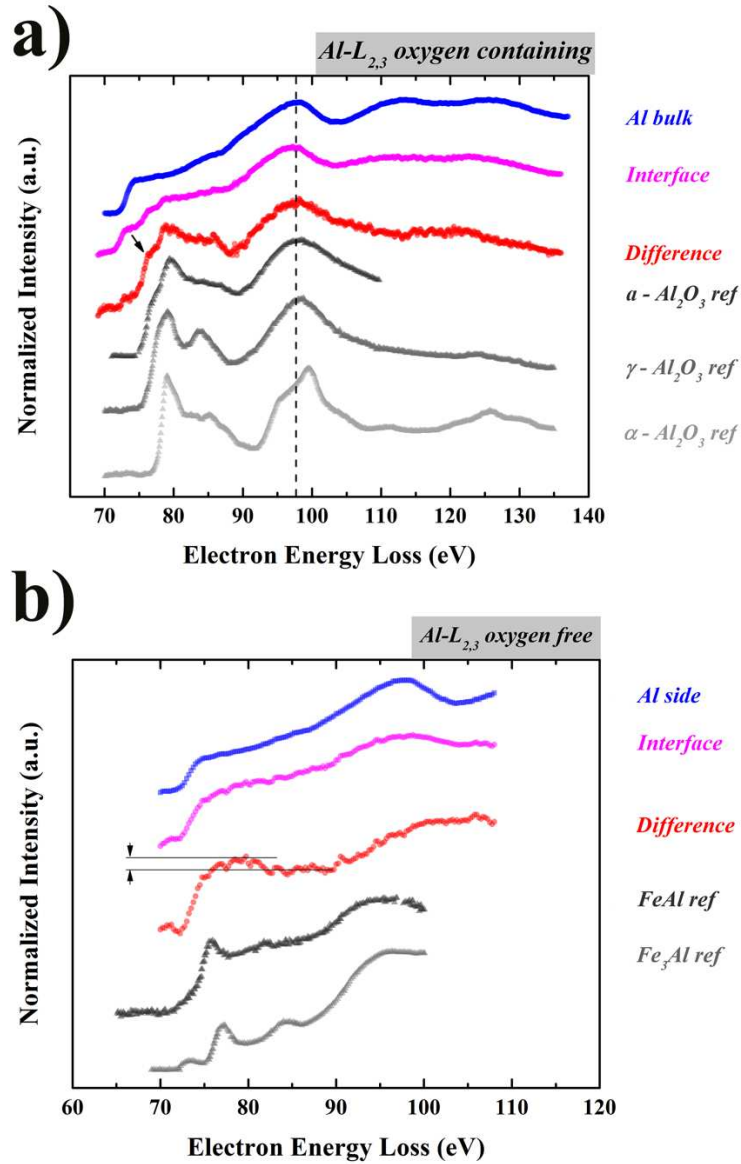


Figure 7: Recorded Al-L_{2,3} spectra of (a) the oxygen containing interfacial area in the Al bulk, at the interface, the corresponding difference spectrum and reference spectra of different Al₂O₃ polymorphs (measured in-house [26]). (b) Al-L_{2,3} edges of the oxygen free interfacial region

recorded on the aluminum side, at the interface, the corresponding difference spectrum and reference spectra for FeAl and Fe₃Al (both references [28]).

Discussion

The present study aims at cold welding of aluminum (EN AW 6082 – 3.2315) and iron (C15 – 1.0401) with an in-depth characterization of bond formation at the interface of the dissimilar materials down to the atomic level. Cold extrusion was used to combine the two billets after adjustment of their respective yield strengths [21].

Our mechanical testing results show that the applied thermal treatment successfully resulted in properly adjusted strengths for the two constituent materials. On average, our site-specific micro tensile tests on positions P1 and P2 were found to be 30 and 60 % below the strength of the monolithic materials (Table 2). However, in these locations the maximum attainable strength was already about 20 % below the monolithic materials. For the micro testing, samples were only accessible in positions with about 50-75 % Al remnants on the fracture surface (Figures 2 & 3). Consequently, the expected site-specific strength is expected to be lower than the maximum strength at positions of highest surface expansion. Previous simulation work of ours revealed a strong correlation between surface enlargement and normal contact stress [17]. In this work, we found that the interfacial bond strength is highest at location P3 of the bi-material joint. In addition, the bond strength follows in these simulations a similar course as captured in the experimental trend observed in the present experiments (Figure 3). As the surface coverage correlates well with the micro tensile strength, the strength of the interface

should be able to exceed the monolithic Al strength in position P3 leading to fracture mainly in the Al bulk rather than at the interface. This failure away from the interface has also been observed in our correlation attempt by simulations, as described above [17]. In summary, our results show that the overall strength of the joints is high by itself, and is likely to exceed the Al bulk strength at areas of highest surface expansion. It has to be noted that the surface preparation to reach high bond strengths is crucial, which is why the etching method was used to obtain highest bond strength [18].

To clarify the origin of the high interfacial bond strength, high-resolution and analytical STEM were combined by support of aberration-correction to clarify the site-specific interface structure, chemical composition (EDS) and local electronic structure (EELS), thereby providing a comprehensive and length-scale bridging picture of interfacial crystallography, phase composition and bond characteristics. For the exact same material system but a slightly different punch geometry as chosen in this study, Altin et al. found that at the interfacial area (P3), in which we expect highest interfacial strength, a significant surface enlargement occurs, the central surface (P1) remains almost in the initial case and the periphery (P5) is only enlarged about 20 % as much as parts of highest enlargement [16]. Such high surface enlargements as reproduced here as well in location P3 should significantly exceed critical enlargements of bond formation models by Bay [9] and Cooper & Allwood [12]. It is consequently expected that mainly Fe and Al contacts are formed during cold welding and only occasionally brittle oxide or work hardened fragments remain along that part of the interface. The presented STEM results of an area of highest surface enlargement (P3) reveal two distinct areas: the

majority of the interface being oxygen free and a smaller oxygen containing area. At the oxygen free part, no intermetallic phase could be found, neither structurally nor chemically. The A2 crystal lattice (Fe-base) extended to the very interface as shown in Figures 4 and 5, respectively. No intermetallic structure was found as atomic column intensity is homogeneous and no super lattice reflections are observed in the corresponding Fourier transform of the image. The lack of atomic column intensity on the Al (dark) side of the interface is indicative for a non-coherent interface, as the chosen HAADF imaging conditions require exact zone axis orientation to reveal atomic column intensity. As there is no common zone axis on the Al-side, no particular orientation relationship exists between both materials after welding. Previous annealing experiments revealed that for dissimilar steel/Al joints detrimental interphase formation occurs above temperatures of about 350°C-450°C either by direct observation [5], or indirectly through the onset of a weakening failure along the interface instead of the bulk [29]. The formation of an intermetallic phase-free interface in the present study thus indicates that the temperatures during welding did not exceed these critical temperatures and that occurring flash temperatures were not sufficient in magnitude or duration to promote intermetallic phase formation.

In the present system, only continuous elemental concentration increases or decreases of both Al and Fe are extracted from the recorded EDS maps, which are inconclusive for phase identification directly at the interface where no phase was apparent from image contrast. Thus, the local electronic structure of the constituent elements in the bulk and at the interface was revealed by EELS measurements. Considering the oxygen free part

of the interface, the Fe-L_{2,3} and Al-L_{2,3} edges are of interest. The former edge recorded at the interface is almost identical to the pure Fe-L_{2,3} edge of the bulk material (Figure 6). This behavior has been reported by Brydson et al. for Fe-Al bonding at Fe/alumina interfaces without presence of an oxygen containing terminating atomic layer [30]. Besides this weak indication of a metal-metal bond in the present study, the changes of the Al-L_{2,3} edge provide much more insight in the actual bonding state by capturing the free electron character of atoms at the interface (Figure 7b). The spatial difference technique reveals an interfacial spectral course that resembles best FeAl according to the shown references by Botton [28]. The observed weak intensity peak at the edge onset (75-80 eV), indicated by arrows, results from reappearance of s-states above the Fermi level caused by hybridization of the Fe *d* bands, which remove the free electron character at the Al sites [28]. Overall, the combination of both effects in the spectra leads to a state in which the interface atoms can only form metal-metal bonds. Especially the emergence of d-states for interfacial atoms reflects the hybridization of Al s- and p-orbitals with Fe d-orbitals, thus contributing to a more covalent bond character between the interfacial atoms and reducing the free electron character [28]. Concluding, our results clearly point towards a more covalent metal-metal (Fe-Al) bond formation by shared hybridized orbitals of Fe and Al at the oxygen free interface portions of highest surface enlargement. Difference spectra of the demonstrated course can only be extracted from areas within two pixels across the interface corresponding to a region of about 0.5 nm wide. Regarding the linear nature of the difference spectrum technique, this indicates atoms of different coordination are only present within one or few atomic planes,

although no atomically resolved EELS was performed. Although Fe-Al bonding occurs directly at the interface, this is not the formation of an intermetallic FeAl phase as it does not fulfil the definition of a “phase”. There is no extended intermetallic FeAl crystal structure formed, nor any other phase within the resolution limit. It has to be noted that a bond environment resembling Fe₃Al cannot be excluded unambiguously with the present bi-material TEM samples, as thickness effects like plasmon excitations might suppress the appearance of characteristic features.

The situation becomes distinctly different in areas where EDS clearly reveals oxygen being present at the interface. The Fe-L_{2,3} edge again looks very close to bulk Fe (Figure 6a). However, compared to the pure Fe edge, the L₃/L₂ white line intensity ratio in the spectrum is increased by about 8 %. According to Brydson et al., this increase of the ratio is related to the presence of oxidized Fe, predominantly Fe²⁺, pointing to the formation of mainly polar Fe-O bonds on one side of the interface [30]. However, the increase of just 8 % is small compared to about 60 % presented by Brydson et al. In addition to the increased L₃/L₂ ratio, a slight shift of the L₃ white line to slightly higher energies, i.e. ~ 0.5 eV was observed as reported in [30]. Regarding the O-K edge (Figure 6b), the presence of Al₂O₃ is demonstrated, as there are no characteristic peaks emerging at around 530 eV energy loss, which would be characteristic for Fe₂O₃ or other oxides (Fe₂O₃ reference adapted from [31]). In terms of crystallinity, the edge onset was found to coincide with the spectrum for a-Al₂O₃ and γ -Al₂O₃, while the onset of α -Al₂O₃ would be expected to shift to slightly higher energy losses. Additionally, the first and second main peaks are connected through a plateau in case of γ -Al₂O₃, while the second peak of

28

amorphous Al_2O_3 appears directly connected to the first peak. A clear double peak would evolve for crystalline $\alpha\text{-Al}_2\text{O}_3$ in this energy loss region [26]. As a result, the investigated interfacial Al_2O_3 resembles most the amorphous Al_2O_3 polymorph. It has to be noted, that differentiating between amorphous $\alpha\text{-}$ and $\gamma\text{-Al}_2\text{O}_3$ is extremely challenging from the O-K edge, as $\gamma\text{-Al}_2\text{O}_3$ is expected to be a defective crystalline oxide with spinel-type structure and a partially disordered cation sublattice [32] that produces an almost identical EELS spectrum to that of an amorphous oxide. However, differentiation is better possible when studying the Al- $L_{2,3}$ edges. As a result, the Al- $L_{2,3}$ edge at the oxygen containing interface portion was further inspected and it was found that it resembles unambiguously the course of the edge for Al bound in amorphous Al_2O_3 in agreement with the findings from the O-K edge. Especially the indicated shoulder of the Al- $L_{2,3}$ edge in Figure 7a) is a strong indication for an amorphous Al_2O_3 , as it has been reported to mainly appear for Al_2O_3 in tetragonal coordination [27]. This is mostly the case in the amorphous polymorph in contrast to octahedral coordination for the respective crystalline polymorphs. Concluding, our results of the oxygen containing interface parts at highest surface enlargements point towards the presence of amorphous aluminum oxide, which is known to form instantaneously as native oxide on pure aluminum surfaces [33]. Al is the stronger reducing agent in presence of oxygen. Therefore, no clear signs of iron oxide formation were found, however, there are indications of few Fe-O bonds forming. Regarding the amorphous material that Fe has to form bonds with, it seems reasonable to postulate only few Fe-O bonds being formed, due to the rather random atomic arrangement at the interface and consequently slightly

differing atomic distances for bond formation, which might be adversely influencing the bond strength further. No apparent signs of bond formation between Fe and Al were found within the experimental framework.

Investigation of the fracture surfaces after extraction (Figure 3), reveals complete detachment of Al at the periphery's interface fraction (P1 – 0.5 % bulk failure in Al) and almost complete detachment in the central region (P5 – 45 % bulk failure in Al). In contrast, at areas of highest surface enlargement (P3), which also contribute most of the load during macroscopic extraction, only Al remnants have been observed (98.7 % bulk failure in Al). Thus, the extraction force was not sufficient to break the interface bonds formed, but rather had the Al fail as weakest part of the dissimilar material joint, in contrast to the periphery and the central portion of the welded joint. These results support the proposed bonding state at the interface. The periphery and central portion do not experience high surface enlargements, and consequently, the Al is most likely almost entirely decorated with amorphous native oxide. As only few Fe-O bonds are established in these regions, extraction forces are low, as only few bonds have to be broken. In contrast, the central portion of highest surface enlargement is mainly held together by covalent Fe-Al bonds at an atomic level at the interface, not an FeAl phase. These strong bonds cover the entire surface at the atomic level and thus contribute to the overall high extraction forces. In fact, these bonds could be even stronger than the Al constituent bulk leading to failure rather in the bulk than at the interface. However, this failure observed might be related to the tensile test geometry. To conclusively proof that the Fe-Al bonds are exceeding the Al-Al bond strength, shear tests of interface

containing samples would be required. It would be interesting to study the influence of crystallinity of aluminum oxide along the interface, as for the Cu/Al₂O₃ system it was shown that spinel formation at the interface increases the strength of itself [34]. That would ensure sufficient bonding not only at points of highest surface enlargements but potentially extend the area towards less enlarged areas as well. Out of the knowledge of atoms participating in a high strength cold pressure welded joint, we summarize schematically an atomistic bonding mechanism that is schematically presented in Figure 8. This suggested mechanism agrees well with our comprehensive experimental EELS, fracture surface and mechanical testing results. Following the different steps are described in detail.

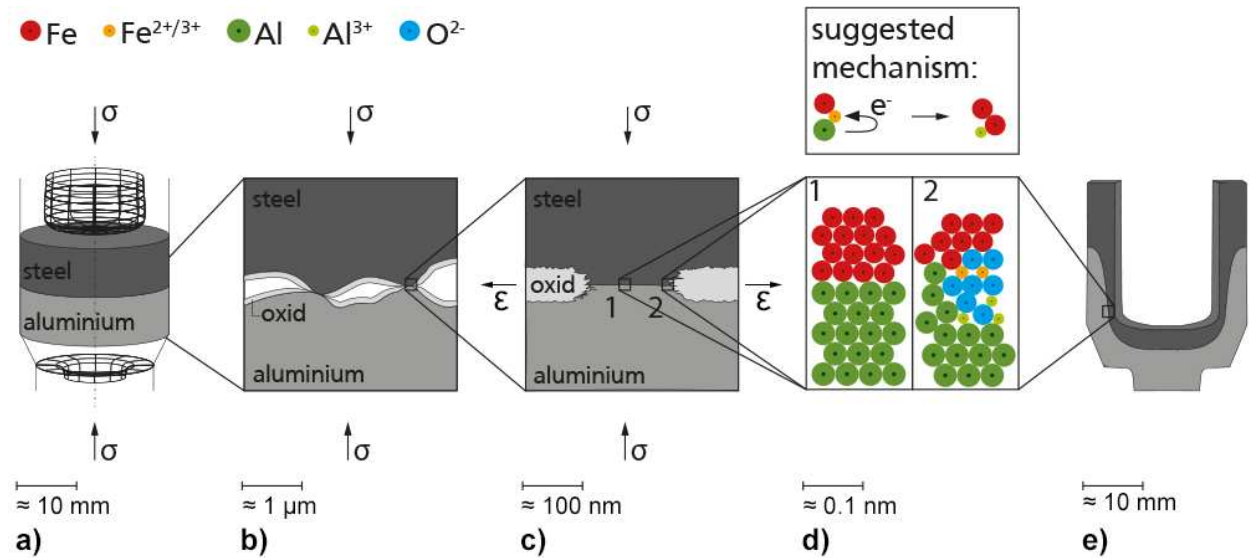


Figure 8: Schematic representation of the suggested atomic bonding mechanism

In the beginning of the forming process (Figure 8a) both the samples to be joined are covered with a thin oxide layer (Figure 8b). On the steel side, there is iron oxide and on the aluminum side amorphous aluminum oxide, both being native oxides hardly

avoidable in ambient conditions. As soon as pressure is applied the surfaces close in and get in contact under high pressures, which occurs first at the micro asperities (Figure 8b). At this point, the forming of the material (plastic deformation) goes along with surface enlargements and eventually initiates the cracking of the brittle oxide layers (Figure 8c). In addition, the persisting pressure forces the juvenile ground material to extrude through the cracks to form new interfaces (Figure 8c). Up to this stage the known model postulated by Bay is followed [9]. Going a step further, our EELS investigation of the final interface (Figure 8e) aimed at a near atomic scale at two different regions: the oxygen rich and the oxygen free area (Figure 8d). The reason for the not measurable appearance of Fe-oxide is that in the vicinity of these ruptured oxides we suggest the following mechanism (Figure 8d-2): Fe ions are reduced to elemental Fe on the expense of the more reactive metallic Al, as expected based on thermodynamic considerations [35]. This process involves the already present oxygen ions as charge carrier. Few Fe-O bonds remain away from the ruptured areas, where Fe, O and Al do not get in close enough proximity or there is not enough juvenile metallic base aluminum extruded through the cracks to initiate the charge transfer process. Further, in areas of high surface enlargements, no oxygen remains and thus elemental Fe and Al get in contact forming a more covalent metal-metal bond under the high pressures involved by sharing their electrons (Figure 8d-1). The formed Fe-Al bond appears stronger than the Fe, O and Al bonding, especially regarding our previous simulation results as well, which show failure in Al away from the interface at locations

of highest surface enlargements [17] and thus indicate low oxide contents. Other bonding states were not detected neither by EDS nor EELS measurements.

Conclusions

Cold forging as a cold welding technique was successfully employed to join a steel (spheroidized C15 – 1.0401) and an aluminum alloy (EN AW6082 – 3.2315-T6) after targeted adjusting heat treatments. Mechanical testing of such interfaces by site-specific tensile experiments revealed that the joint strengths are increase along the interface up to about 60 % of the constituent strength and is expected to be highest on areas not accessible for tensile testing but exhibiting highest surface enlargements. This is deduced from SEM images of the fracture surfaces. Aberration-corrected STEM in combination with EELS were employed to clarify bond formation at these dissimilar material interfaces leading to the observed beneficial integrity. The experiments presented here show evidence for large areas lacking both oxides and intermetallic phases in areas of highest surface enlargements. Instead, Fe-Al bonds with a more covalent character were formed at the interface without forming the corresponding intermetallic phase as the critical conditions for its formation were not yet reached. These strong bonds prevent interfacial failure. In contrast, few areas with presence of oxides exist as well. Experiments discussed here show amorphous aluminum oxide remnants that form only few polar Fe-O bonds, due to their amorphous nature. Consequently, these strong ionic bonds cannot contribute to the overall joint strength enough compared to the prevailing Fe-Al bonds of the oxygen-free areas. Out of these findings, an atomistic and thus

extended picture of the bond formation model is suggested, which is based on the near atomic level characterization of a cold pressure welded bond and extends Bay's model.

Acknowledgments

The authors acknowledge the DFG (Deutsche Forschungsgemeinschaft) for funding via the subprojects ER 601/3-1, ER 601/3-2 and GR 1818/48-2, GR 1818/48-3 within the priority program 1640 "Joining by plastic deformation".

References

- [1] C. Yao, B. Xu, X. Zhang, J. Huang, J. Fu, Y. Wu, Interface microstructure and mechanical properties of laser welding copper–steel dissimilar joint, *Opt. Lasers Eng.* 47 (2009) 807–814. doi:10.1016/j.optlaseng.2009.02.004.
- [2] Y.F. Sun, H. Fujii, N. Takaki, Y. Okitsu, Microstructure and mechanical properties of dissimilar Al alloy/steel joints prepared by a flat spot friction stir welding technique, *Mater. Des.* 47 (2013) 350–357. doi:10.1016/j.matdes.2012.12.007.
- [3] U. Dilthey, *Schweißtechnische Fertigungsverfahren 2: Verhalten der Werkstoffe beim Schweißen*, Springer-Verlag, 2006.
- [4] E.T. Akinlabi, A. Andrews, S.A. Akinlabi, Effects of processing parameters on corrosion properties of dissimilar friction stir welds of aluminium and copper, *Trans.*

Nonferrous Met. Soc. China. 24 (2014) 1323–1330. doi:10.1016/S1003-6326(14)63195-2.

[5] H. Springer, A. Kostka, J.F. dos Santos, D. Raabe, Influence of intermetallic phases and Kirkendall-porosity on the mechanical properties of joints between steel and aluminium alloys, Mater. Sci. Eng. A. 528 (2011) 4630–4642. doi:10.1016/j.msea.2011.02.057.

[6] V.R. Riabov, Aluminizing of steel, Oxonian Press, 1985.

[7] M. Zamanzade, A. Barnoush, C. Mot, A Review on the Properties of Iron Aluminide Intermetallics, Crystals. 6 (2016) 10. doi:10.3390/cryst6010010.

[8] K. Mori, N. Bay, L. Fratini, F. Micari, A.E. Tekkaya, Joining by plastic deformation, CIRP Ann. 62 (2013) 673–694. doi:10.1016/j.cirp.2013.05.004.

[9] N. Bay, Cold Pressure Welding—The Mechanisms Governing Bonding, J. Eng. Ind. 101 (1979) 121–127. doi:10.1115/1.3439484.

[10] N. Bay, Cold pressure welding - basic parameters and applications, Proceed. Int. Conf. Join. Met. 1. (1981) 71–78.

[11] N. Bay, Cold pressure welding - a theoretical model for the bond strength, Proceed Instn Met. Spring Res Conf Join. Met. Pract. Perform. (1981) 47–62.

[12] D.R. Cooper, J.M. Allwood, The influence of deformation conditions in solid-state aluminium welding processes on the resulting weld strength, J. Mater. Process. Technol. 214 (2014) 2576–2592. doi:10.1016/j.jmatprotec.2014.04.018.

- [13] C.Y. Barlow, P. Nielsen, N. Hansen, Multilayer roll bonded aluminium foil: processing, microstructure and flow stress, *Acta Mater.* 52 (2004) 3967–3972. doi:10.1016/j.actamat.2004.05.012.
- [14] R. Marstatt, M. Krutzlinger, J. Luderschmid, M.F. Zaeh, F. Haider, Formation of a diffusion-based intermetallic interface layer in friction stir welded dissimilar Al-Cu lap joints, *IOP Conf. Ser. Mater. Sci. Eng.* 181 (2017) 012002. doi:10.1088/1757-899X/181/1/012002.
- [15] C. Wang, Y. Jiang, J. Xie, D. Zhou, X. Zhang, Interface formation and bonding mechanism of embedded aluminum-steel composite sheet during cold roll bonding, *Mater. Sci. Eng. A.* 708 (2017) 50–59. doi:10.1016/j.msea.2017.09.111.
- [16] A. Altin, S. Wohletz, W. Krieger, A. Kostka, P. Groche, A. Erbe, Nanoscale understanding of bond formation during cold welding of aluminum and steel., *Adv. Mater. Res.* 966-967 (2014) 445-452. doi:10.4028/www.scientific.net/AMR.966-967.445
- [17] S. Wohletz, *Erzeugung stoffschlüssiger Verbunde durch Kaltfließpressschweißen*, Shaker, Aachen, 2017.
- [18] S. Wohletz, P. Groche, Temperature influence on bond formation in multi-material joining by forging, *Procedia Eng.* 81 (2014) 2000–2005.
- [19] P. Groche, S. Wohletz, A. Erbe, A. Altin, Effect of the primary heat treatment on the bond formation in cold welding of aluminum and steel by cold forging, *J. Mater. Process. Technol.* 214 (2014) 2040–2048. doi:10.1016/j.jmatprotec.2013.12.021.

- [20] P. Groche, S. Wohletz, M. Brenneis, C. Pabst, F. Resch, Joining by forming—A review on joint mechanisms, applications and future trends, *J. Mater. Process. Technol.* 214 (2014) 1972–1994. doi:10.1016/j.jmatprotec.2013.12.022.
- [21] P. Groche, S. Wohletz, A. Mann, M. Krech, V. Monnerjahn, Conjoint Forming - Technologies for Simultaneous Forming and Joining, *IOP Conf. Ser. Mater. Sci. Eng.* 119 (2016) 012025. doi:10.1088/1757-899X/119/1/012025.
- [22] C. Scheu, W. Stein, M. Rühle, Electron Energy-Loss Near-Edge Structure Studies of a Cu/(11-20) α -Al₂O₃ Interface, *Phys. Status Solidi B.* 222 (2000) 199–211. doi:10.1002/1521-3951(200011)222:1<199::AID-PSSB199>3.0.CO;2-2.
- [23] S. Zhang, C. Scheu, Evaluation of EELS spectrum imaging data by spectral components and factors from multivariate analysis, *Microscopy.* 67 (2017) i133–i141.
- [24] A. Feldhoff, J. Martynczuk, M. Arnold, M. Myndyk, I. Bergmann, V. Šepelák, W. Gruner, U. Vogt, A. Hähnel, J. Woltersdorf, Spin-state transition of iron in (Ba_{0.5}Sr_{0.5}(Fe_{0.8}Zn_{0.2})O_{3- δ}) perovskite, *J. Solid State Chem.* 182 (2009) 2961–2971. doi:10.1016/j.jssc.2009.07.058.
- [25] G. Botton, G. Guo, W. Temmerman, C. Humphreys, Experimental and theoretical study of the electronic structure of Fe, Co, and Ni aluminides with the B2 structure, *Phys. Rev. B.* 54 (1996) 1682.
- [26] S.W. Hieke, G. Dehm, C. Scheu, Annealing induced void formation in epitaxial Al thin films on sapphire (α -Al₂O₃), *Acta Mater.* 140 (2017) 355–365.

doi:10.1016/j.actamat.2017.08.050.

[27] V. Edlmayr, T. Harzer, R. Hoffmann, D. Kiener, C. Scheu, C. Mitterer, Effects of thermal annealing on the microstructure of sputtered Al₂O₃ coatings, *J. Vac. Sci. Technol. Vac. Surf. Films.* 29 (2011) 041506.

[28] G.A. Botton, Eels Near Edge Structures, in: D.G. Rickerby, G. Valdrè, U. Valdrè (Eds.), *Impact Electron Scanning Probe Microsc. Mater. Res.*, Springer Netherlands, Dordrecht, 1999: pp. 265–300. doi:10.1007/978-94-011-4451-3_11.

[29] K. Mechsner, H. Klock, Grenzflächengefüge von Reibschweissverbindungen aus Aluminium und Stahl, *Aluminium.* 59 (1983) 850–854.

[30] R. Brydson, J. Bruley, H. Müllejans, C. Scheu, M. Rühle, Modelling the bonding at metal-ceramic interfaces using PEELS in the STEM, *Ultramicroscopy.* 59 (1995) 81–92. doi:10.1016/0304-3991(95)00020-2.

[31] S.-Y. Chen, A. Gloter, A. Zobelli, L. Wang, C.-H. Chen, C. Colliex, Electron energy loss spectroscopy and ab initio investigation of iron oxide nanomaterials grown by a hydrothermal process, *Phys. Rev. B.* 79 (2009) 104103. doi:10.1103/PhysRevB.79.104103.

[32] I. Levin, D. Brandon, Metastable Alumina Polymorphs: Crystal Structures and Transition Sequences, *J. Am. Ceram. Soc.* 81 (1998) 1995–2012. doi:10.1111/j.1151-2916.1998.tb02581.x.

[33] H.M. Dunlop, M. Benmalek, Role and Characterization of Surfaces in the

Aluminium Industry, *J. Phys.* IV. 07 (1997) C6-163-C6-174. doi:10.1051/jp4:1997614.

[34] G. Katz, Adhesion of copper films to aluminum oxide using a spinel structure interface, *Thin Solid Films*. 33 (1976) 99–105. doi:10.1016/0040-6090(76)90591-5.

[35] John R. Rumble (ed.), *CRC Handbook of Chemistry and Physics*, 99th edition (Internet Version), CRC Press/Taylor & Francis, Boca Raton, 2018.